2. A New Global Database of Mars Impact Craters to 1 km: 1. Database Creation, Properties, and Parameters

Note: This paper is in preparation as: Robbins, S.J., and B.M. Hynek. "A New Global Database of Mars Impact Craters to 1 km: 1. Database Creation, Properties, and Parameters." (in prep. for Icarus). Though it has not yet been submitted, it is cited in this dissertation as "Robbins and Hynek, 2011b." Sections have been re-numbered and some reformatting has been done to fit the formatting of the rest of this dissertation. References have been combined with all others at the end of this dissertation. Acknowledgments have been combined with others at the beginning of this dissertation.

Abstract: Impact craters have been used as a standard metric for a plethora of planetary applications for many decades, including age-dating, geologic mapping and stratigraphic relationships, as tracers for surface properties, and as locations for sampling lower crust and upper mantle material. Utilizing craters for these and other applications is significantly aided by a uniform catalog of craters across the surface of interest. Consequently, catalogs of craters have been developed for decades for the moon and other planets. We present a new global catalog of Martian craters statistically complete to diameters $D \geq 1$ km. It contains 378,540 craters, and for each crater it lists detailed positional, interior morphologic, ejecta morphologic and morphometric, and modification state information. In this paper, we detail how the database was created, the different fields assigned, and statistical uncertainties and checks. In our companion paper (Robbins and Hynek, 2011c, this volume), we discuss the first broad science applications and results of this work.

2.1. Introduction

Since Galileo first turned his telescope to the moon and identified the three-dimensionality of craters (Galilei, 1610), people have been cataloging craters on the solar system's solid bodies. Some of the first modern crater catalogs were generated in preparation for the *Apollo* missions in the 1960s with other geomorphologic features (*e.g.*, Kuiper, 1960; Schimerman, 1973), followed by more methodic and global catalogs in the subsequent decades (Pike, 1977, 1988 and references therein; Wood and Andersson, 1978). When the first images of Mars were returned by *Mariner 9*, craters were cataloged there, as well. The first global crater database of Mars was created by Nadine Barlow, published two decades ago (Barlow, 1988), and it contained all 42,284 craters with diameters $D \geq 5$ km identifiable from *Viking* images. The database contains the locations and diameters of craters along with basic morphology, though it is referenced in the Mars Digital Image Model 1.0 (MDIM 1.0) and hence crater locations are no

longer accurate in the present MDIM 2.1. Nonetheless, this has stood as a reference set for the past two decades and is distributed as a standard package with other Mars datasets by the United States Geological Survey (USGS).

Since that time, higher-quality and -resolution imagery has been taken of Mars, as has topographic data, which can be used to produce a new generation of a Mars crater catalog. Barlow is in the process of updating the "Catalog of Large Martian Impact Craters" (*e.g.*, Barlow, 2003), which will update the locations and diameters, remove false positives, and include some missed craters $D \geq 5$ km from the original catalog; it will also include topography information, more morphology, and a more detailed degradation state (c.f. Barlow, 2004 for a discussion of degradation state). Besides manual identification methods, automated approaches have been made to cataloging Martian impact craters. Notably, Stepinski *et al.* (2009) published a catalog stated to be complete to roughly $D \sim 3$ km (see Section 2.7.5.2). It was created by purely automated machine-learning techniques utilizing the *Mars Global Surveyor*'s Mars Orbiter Laser Altimeter (MOLA) data (Zuber *et al.*, 1992; Smith *et al.*, 2001). It contains the locations, diameters, and depths of all identified craters, approximately 79,000. Since MOLA data were used to define MDIM 2.1, the Stepinski *et al.* (2009) catalog is in the MDIM 2.1 system. An additional meta-approach has been used to combine existing crater catalogs into a single database and location (*e.g.*, Salamunićcar *et al.*, 2011). This method relies upon a computer algorithm to match craters across input databases and return an average location and size. These are subject to manual checking. This has resulted in a database with ~129,000 craters (see Section 2.7.5.3).

While global crater catalogs are perhaps the most useful, local or type ones have been generated for Mars' craters since the first imagery was returned over four decades ago. These have been amassed with different purposes for each one. A distinct advantage of smaller catalogs is they can go into greater detail in terms of morphologic and morphometric crater properties due to the shear time involved for each crater. Examples of global type catalogs are usually limited to fresh craters (*e.g.*, Roddy *et al.*, 1998; Boyce and Garbeil, 2007), though some

are incredibly specialized, such as a catalog that only includes crater-exposed bedrock (Tornabene *et al.*, 2010).

We are delivering an independently created Martian crater catalog with 378,540 craters complete to diameters $D \geq 1.0$ km, though we possess and will distribute the additional ~250,000 craters used to ensure this completeness on an individual basis upon request. All craters were manually identified and measured as discussed in Section 2.2. The catalog also contains detailed topographic information (Section 2.3), interior morphology including degradation state and whether the crater is a secondary (Section 2.4), ejecta morphology (Section 2.5), and ejecta morphometry (Section 2.6). We discuss the completeness of the current release of this database in Section 2.7, and science results are laid out in our companion paper, this volume: "A New Global Database of Mars Impact Craters to 1 km: 2. Global and Regional Properties and Variations, and Their Implications to Surface Properties and Gravity Scaling." Appendix A lists all the parameters found in this database.

2.2. Crater Identification and Position, Diameter, and Ellipse Parameter Measurements

The bulk of crater identification and classification was done using THEMIS Daytime IR planet-wide mosaics (Christensen *et al.*, 2004). The THermal EMission Imaging System (THEMIS) aboard the *2001 Mars Odyssey* NASA spacecraft is a multi-spectral thermal-infrared imager, sensitive to wavelengths between 0.42-0.86 μm and 6.8-14.9 μm. The bands were chosen to be sensitive to mineralogy of interest to the Mars Exploration Program (*e.g.*, carbonates and hydrothermal silica). One of the initial goals for the instrument was to create a global mosaic of the planet at 100 m/pix in both day and night from which - among a broad array of applications - thermal inertia maps could be calculated. The average local time for daytime observations is 4:30 P.M. to yield a high phase angle with shadows and heating effects sufficient for geomorphologic feature identification.

As of this writing in early 2011, the instrument and spacecraft are still in operation, continuing to provide data nine years after orbit insertion. Mosaic revision from the stream of

returned images is still being done, though the public release cycle is much less frequent. The current public version was released on June 23, 2010, at 100 m/pix from the band centered at 12.57 μm. It has roughly ~99% global coverage of usable data with the largest gaps in the high northern latitudes. The mosaics are constructed from a semi-controlled net to the MOLA basemap (Hare, pers. comm.). This results in small offsets when compared with MOLA in some areas in the present release of a maximum of ~1 km, though there is image doubling in some areas due to the lack of a complete control net and blending.

In *ArcGIS* software, THEMIS Daytime IR mosaics were used to manually locate all visible craters with diameters $D\gtrsim1$ km in approximate local coordinate systems. The THEMIS Daytime IR dataset initially used covered ~90% of the planet at 256 pix/deg resolution (230 m/pix at equator). In August 2010, the new THEMIS mosaics at 100 m/pix were used for the final stages of the database and all morphology; THEMIS data are publicly available through USGS's PIGWAD website. Global mosaics were searched a total of four times for craters to ensure as complete a database as possible. The final search was the only search made with the June 2010 data release.

Crater identification was accomplished using *ArcGIS*'s editing tools to draw a polyline that traced the visible rim of each crater. Partial rims were only identified for the parts that were visible. Polylines were created with vertex spacing of approximately 500 m such that each representative rim ideally consists of $\sim2\pi D$ vertices where D is the crater diameter (see Fig. **3**). All vertices were saved as double-precision points in decimal degrees units. Analysis of all polygons was completed in *Igor Pro* software due to its advanced data visualization capabilities and familiarity with its built-in programming language.

The initial crater search used both THEMIS and Viking maps. Most latitudes were searched in the standard Mercator cylindrical projection while those poleward of ±65° were searched in a polar stereographic projection. The second search was done in the same manner except the on-screen scale was decreased to identify possible missed larger craters. The third search relied upon MOLA topographic maps at the highest resolution available (up to 1/512° per

pixel at the poles (14 m/pix at 70° latitude), 1/128° per pixel equator-ward of ~65-70° latitude (463 m/pix at 0° latitude)) to identify craters that may have a topographic signature but not an obvious visual one (similar to "quasi-circular depressions" (Frey *et al.*, 2002) though Frey *et al.* do not claim that all identified features are craters). From the first two searches, 286,623 craters had been identified, and an additional 5,651 craters were identified with the MOLA search. While this represents an increase of only 1.97%, it represents an increase of 4.06% for craters $D \geq 5$ km, indicating that inclusion of topographic data in crater identification is an important tool.

The final search was completed at significantly higher on-screen scale due to the increased fidelity of the new THEMIS Daytime IR mosaics that were used exclusively for this step. Up to this point, the goal for the database had been to be statistically complete to 1.5-km-diameter craters. However, a large portion of the planet was complete to ~1.25 km while regions near the north pole were closer to ~3.0 km; the higher resolution mosaics available allowed the final search to succeed in bringing statistical completeness across the entire planet to D~1.0 km (Fig. **4**). Statistical completeness in this work is defined numerically from an incremental size-frequency plot; the diameter bin D greater than the diameter bin with the largest number of craters is considered to be the statistical completeness size (see Section 2.7.1). Due to the increased THEMIS resolution as well as the smaller crater sizes examined, the resolution at which vertices were laid down was increased by a factor of $2\times$ to 1 point every 250 meters. 25% of the planet was searched again after this pass to verify completeness of identified craters.

2.2.1. Circle Fitting

All crater polylines were read into an *Igor Pro* file and fitted with a custom-written non-linear least-squares (NLLS) circle fitting routine. The basic theory behind a NLLS algorithm is to guess the parameters that best fit the data and then successively refine them by calculating the difference between the equation being fitted with those parameters and the actual data. For a circle, with three parameters (center x, center y, and radius), the initial guesses do not have to be accurate but should be non-zero. The algorithm employed started by converting the decimal deg-
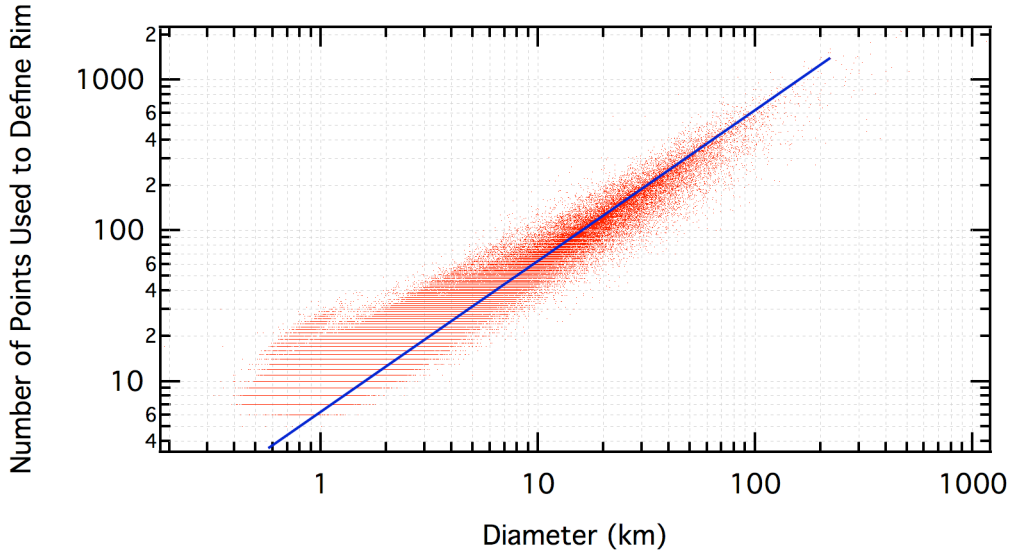
Figure 3: Number of points used to define each crater versus the crater diameter. Blue line is $2\pi D$. Points below the blue line are mostly due to only partial rims that are visible on the planet today. Points above the blue line are due to both occasional circling of craters twice to better-define the rim (especially at small diameters) and due to projection effects away from the equator. The cluster of points above the line around $D \approx 1$ km is from the final search where vertex resolution was increased to one point every 250 m. Posterization in the lower right is due to discrete points being used and the nature of logarithmic plots.
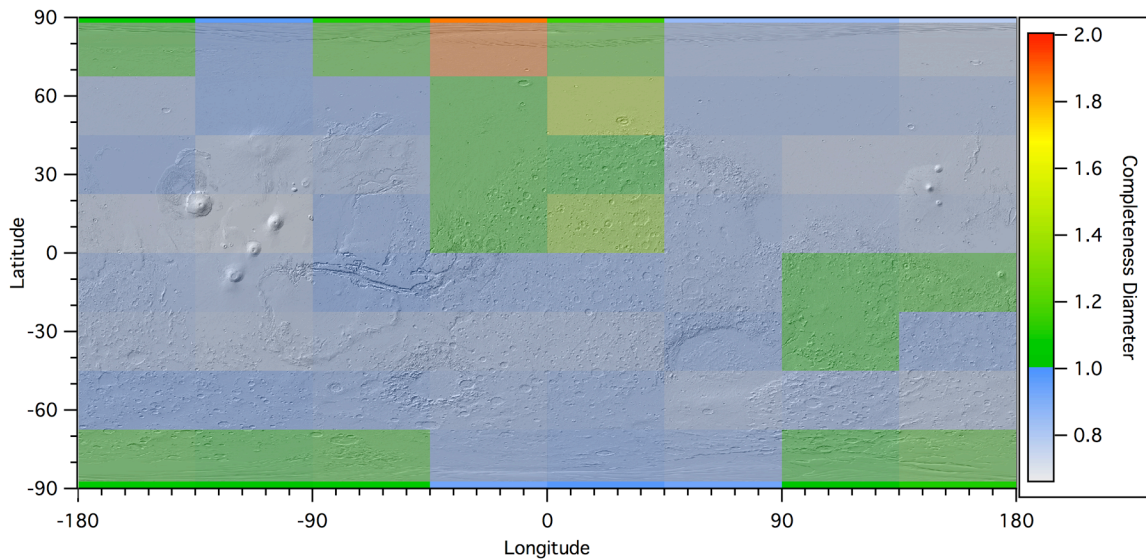

Figure 4: Color-coded area plot showing statistical completeness of crater diameters across the planet (see Section 2.7.1). Bins are 22.5° latitude by 45° longitude resolution. Finer resolution gives skewed results near the poles due to small number statistics. The low completeness in the bin centered at 78.75°N, -22.5°E is due to the young, large Lomonosov impact crater and the north polar cap, and the one centered at 56.25°N, 22.5°E is due to the similarly young, large Lyot impact crater. This is discussed further in Section 2.7.1.

rees of a crater's vertices into kilometers from the center of mass (the average of all x values and y values), eliminating all first-order projection effects. The vertices were then fit with the NLLS circle algorithm that saved the best-fit center latitude and longitude as well as the circle's radius. Latitude and longitude were converted back into decimal degrees, and the radius was multiplied by 2 and saved as the diameter. Uncertainties in the fit parameters were also saved (see Section 2.2.4).

2.2.2. Ellipse Fitting

Ellipse fitting was done by another custom-written NLLS algorithm in *Igor Pro*. There were five free parameters in this fit: a is the semi-major axis, b the semi-minor axis, x_0 the center longitude, y_0 the center latitude, and θ is the tilt of the ellipse's major axis. Ellipse fits to an arbitrary tilt in Cartesian coordinates are unstable because the partial derivatives are dependent upon either the inverse-square or -cube of the semi-major and -minor axes (see Appendix B). If a or b become small, the fit will rapidly approach infinity; if they become large, the fit will approach 0. An intelligent guessing of the major and minor axes was employed by taking the average of the maximum minus the minimum of the crater's longitudinal (x) and latitudinal (y) extents. These were multiplied by a random number drawn from a Gaussian distribution with $\mu = 1.0$ and $\sigma = 0.25$ and saved as the initial guesses for the major and minor axes. The tilt angle initial guess was drawn from a uniform distribution between $\pm\pi$ relative to a long axis oriented along a North-South line. Parameters were monitored during each fit iteration to verify they did not become too large nor small, and the fit was re-done up to five times with the requirement that it converged upon identical parameters at least three times (this is discussed in greater detail in Appendix B). If the fit converged, the crater's center latitude and longitude were recorded along with the major and minor axes, tilt angle, eccentricity e, and ellipticity ε. Eccentricity was calculated as $e = \sqrt{1 - b^2/a^2}$ and ellipticity is defined as $\varepsilon = a/b$.

2.2.3. Uncertainties in Crater Measurements

Because every crater was traced by hand and not by an unbiased (or uniformly biased) computer algorithm, there was a certain amount of random uncertainty inherent in every vertex identified. At the most basic level, an uncertainty of ±0.5 px was present based upon the limits of the data even if crater rim-tracing was perfect (~115 m at the equator for the first two searches, ~233 m at the equator for the third, and ~50 m at the equator for the final). There is also an inherent error in the digitization of an ellipse, and this is discussed in Section 2.2.4. Besides these two factors which can be estimated from theory, there was additional human error in the accuracy of each tracing.

The human error followed a Gaussian distribution about the true rim for a crater of a given size as measured by the residuals from numerous crater fits. This Gaussian was modeled from a sampling of ~40,000 craters via the following method: (1) After fitting a circle to a crater, the radial distance of each identified vertex was subtracted from the fitted circle radius. (2) The standard deviation of these residuals for each crater was calculated. (3) These standard deviations versus the crater diameter were fit to a power-law which modeled well the distribution, where the fit was of the form $\xi = y_0 + A \cdot x^p$ where ξ is the recorded value; y_0, A, and p are fit parameters; and x is the "true" location of the vertex. The fit parameters were calculated to be $y_0 = 0.015 \pm 0.001$, $A = 0.024 \pm 0.000$, and $p = 0.938 \pm 0.003$.

To understand the effects of this on the final crater database, an ideal circle of different diameters was modeled with each size having $2\pi D$ vertices. To the x and y value of each vertex, random noise drawn from a Gaussian distribution was added where the standard deviation of that Gaussian was given by the modeled power-law described above. For example, a $D = 5$ km crater was modeled to have a standard error in each vertex of ~±0.12 km. A Monte Carlo set of simulations both fitting a NLLS circle and ellipse to the model crater was run. The ratio of the fitted diameter versus the true diameter of the circle fit was recorded as was the ellipticity ε as a tracer of the uncertainty in the ellipse fit. This simulation was performed for 10,000 craters each at diameter between 1.0 and ~53 km in multiplicative intervals of $2^{1/4}D$.
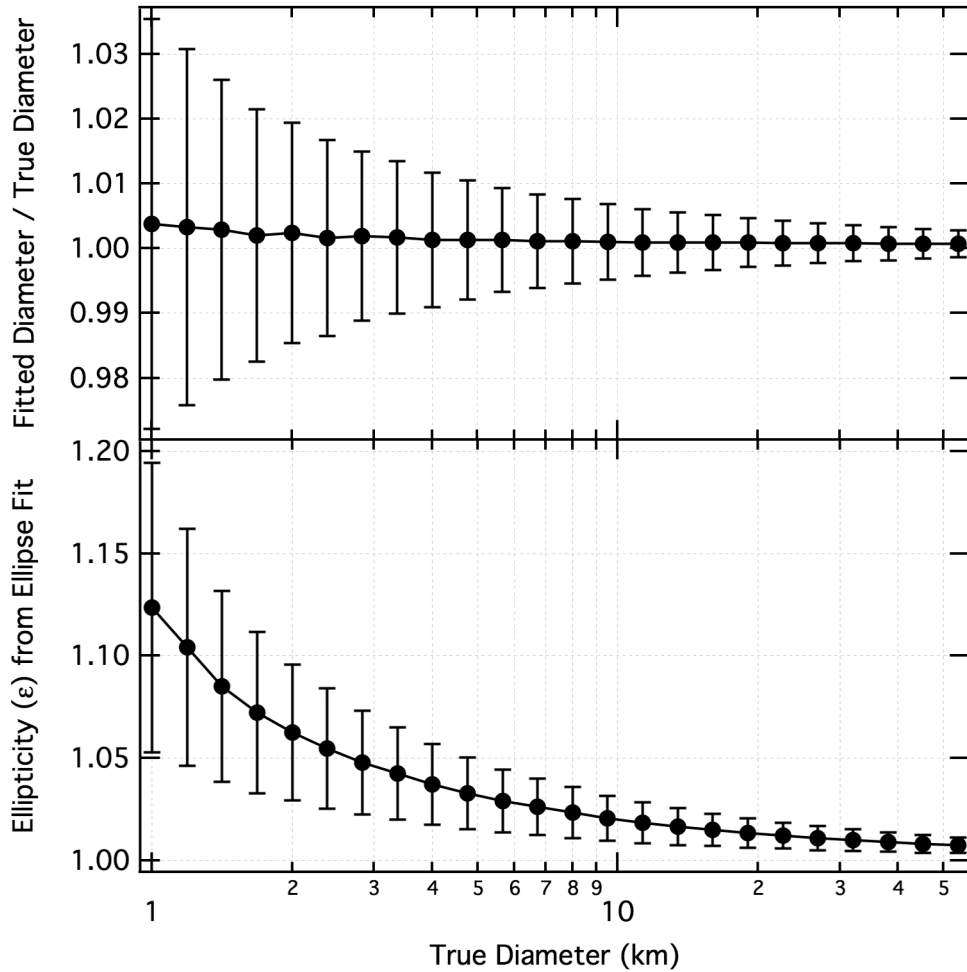
Figure 5: Both panels show the results of Monte Carlo simulations using the NLLS circle and ellipse on a "noisy" circular crater model. Ten thousand simulations for each diameter point were conducted (1.0-53 km in $2^{1/4}D$ multiplicative intervals), and the mean and standard deviation of the results are shown (at larger diameters, error bars are smaller than the symbol size). Top - Deviation of the circle-fit diameter from the true model diameter, where 1.00 would be a perfect match. Bottom - ε, which should be 1.00 for the modeled circle.

The mean and standard deviation of each simulation set of circle diameters were recorded and plotted against the true diameter (Fig. **5**, top panel). A very small aliasing of 0.4% was present at the smallest diameters. For $D = 1$ km, the Monte Carlo simulations show the NLSS fit is 100.4±3.2% of the true diameter with this noise model; it drops to <100.1% for $D \gtrsim 10$ km, and the $\mu \pm \sigma$ range of the fits was within the true diameter for all crater ranges examined. It should be noted that this is an over-estimate for most of the small craters since the majority of $D \sim 1$ km craters were identified in the final search at higher resolution - both imagery and on-screen

display. A comparable model is run for the increased resolution of the final crater identification (noise model: $\xi = (-0.009 \pm 0.000) + (0.041 \pm 0.000) \cdot x^{0.781 \pm 0.003}$). The $D = 1$ km value is 100.3±2.8%.

The ellipticity ε should be 1.0 for all cases (*a* and *b* should be the same) if the fit were perfect and the noise level 0%. The mean and standard deviation of $\varepsilon(D)$ are shown in Fig. **5**, bottom panel. Fits to smaller craters were significantly different from their true values as expected based on the following thought experiment: A 1.0-km-diameter crater will have approximately 6 vertices and be 5 pixels across. If one of those vertices is 1 pixel "outside" of the true circle, while another is 1 pixel "inside," a ~6 by 4-px ellipse results with $\varepsilon = 1.5$; it will be less if the offsets are not two vertices apart. Therefore, it is incredibly "easy" to get large ellipticities from such small craters simply due to very small errors in tracing. ε fell below the 1.1 level for $D \gtrsim 1.5$ km, and it fell below the 1.05 level for $D \gtrsim 2.5$ km.

An alternative way of presenting these data is how likely the ellipse fit resulting in a value ε is a true representation of that value for a stated *a priori* confidence level. This can be done by creating a histogram of the Monte Carlo results for each diameter test and calculating a
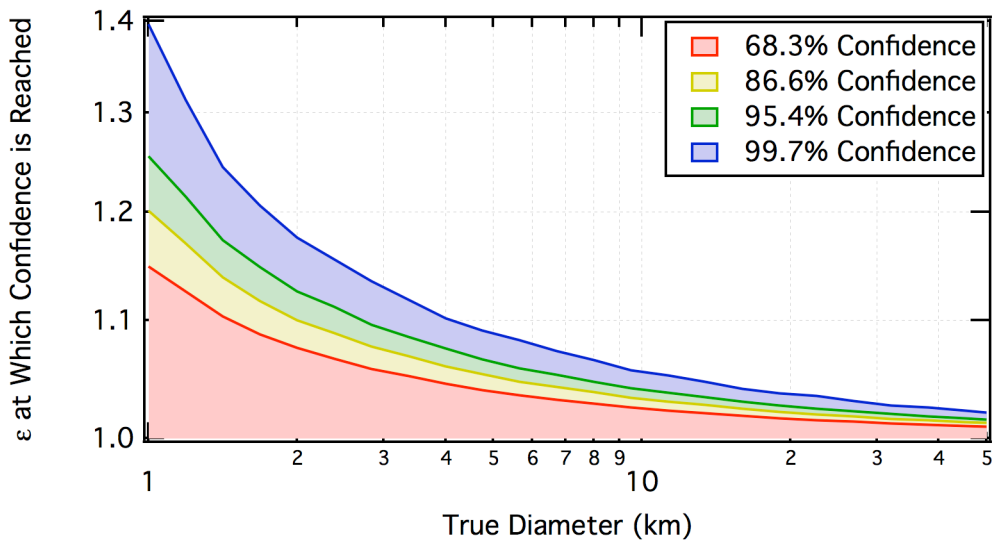

Figure 6: For the uncertainty model described in the text, the shaded regions represent all ε at which the confidence that the fitted ε is a true representation of the crater's ε for a given confidence level. For example, if one wanted to state with 95.4% confidence (2σ) that a $D = 2$ km crater had a certain ε value, they could only do so for $\varepsilon > 1.44$ from this database.

cumulative probability distribution from it. The ε value at which the fraction of simulations is equal to the confidence level is then determined. This was graphed for 68.3%, 86.6%, 95.4%, and 99.7% confidence levels in Fig. **6** (corresponding to 1, 1.5, 2, and 3σ in a Gaussian distribution). From this Figure, a crater diameter must be $D > 2.2$ km for the confidence to be 68.3% that a derived $\varepsilon < 1.1$ is a true reflection of the crater. $D > 4.0$ km, >5.7 km, and >8.2 km are the requisite diameters for the 86.6%, 95.4%, and 99.7% confidence levels, respectively.

2.2.4. Uncertainties in Circle-Fit Parameters

A FORTRAN95 code released as "ODRPACK95" by Zwolak *et al*. (2004) is incorporated into the *Igor Pro* software. It can analytically calculate uncertainties for implicit functions (functions that are not a simple function *y* of *x*) was used. This package was incorporated into the NLLS circle-fitting algorithm discussed above to calculate formal uncertainties in the fitted central latitude and longitude and the circle's diameter. These are found in the catalog (see Appendix A). The uncertainties relative to the crater diameter were plotted, and the results were binned in multiplicative intervals of $2^{1/16}D$. A piece-wise power-law function (Eq. 2) describes the uncertainty:

$$\delta D = A \cdot D^p \begin{cases} A = 0.017 \pm 0.004, \ p = 0.531 \pm 0.058 \ , 5.78 \leq D \leq 150 \text{ km} \\ A = 0.032 \pm 0.009, \ p = 0.121 \pm 0.250 \ , 1.50 \leq D \leq 5.78 \text{ km} \\ A = 0.023 \pm 0.004, \ p = 1.122 \pm 0.862 \ , 0.86 \leq D \leq 1.50 \text{ km} \end{cases} \tag{2}$$

where δD is the uncertainty in km for a given crater diameter D in km. This can be applied in the following examples: The average fit uncertainty $\delta D(D = 1 \text{ km}) = \pm 0.02$ km (2%), $\delta D(D = 5 \text{ km}) = \pm 0.04$ km (1%), $\delta D(D = 10 \text{ km}) = \pm 0.06$ km (0.6%), and $\delta D(D = 50 \text{ km}) = \pm 0.14$ km (0.3%). These formal uncertainties may appear somewhat small, but analytically they are the best estimates from the data of what the uncertainty *from the fit* to each crater. Additionally, analysis of several craters with higher-resolution imagery resulted in very similar diameters with a general deviation at the ~few-percent level. Examination of these relative to the power-law of the mean of a Gaussian uncertainty in the circle fits from Section 2.2.3 suggests similar values at small diameters, but values closer to ~1% for $D > 10$ km. These are about an

order of magnitude smaller than the quoted uncertainty in the Barlow (1988) database of $\sim\pm10\%$.

Finally, there is a theoretical uncertainty from simple digitization: When a continuous shape is discretely digitized, a resolution-dependent uncertainty results, similar to that discussed in Section 2.2.3. This is described by Sladoje and Žunić (1997), who found that with ellipses of approximately this size with the lower resolution at $D\sim1$ km, the absolute error is on the order of $\sim10\%$. At resolutions corresponding to craters $D\sim10$s km, the absolute error is on the order of 1% or less. Since this is generally comparable to the fitted errors overall from ODRPACK95, the numerical method from the data was used as opposed to the theoretical one from Sladoje and Žunić (1997).

2.3. Determining Crater Topographic Properties

One key difference between this extensive database and the current public Barlow catalog is the inclusion of a myriad of topographic properties. Only in the past decade has wide-spread planetary topography been available for Mars, making a uniform derivation of rim heights, surface elevation, and crater floor depth possible (Smith *et al.*, 2001). The Stepinski *et al.* (2009) catalog includes depth information from an automated method, while that information was derived manually for this catalog and is being manually derived for Barlow's revised catalog (pers. comm.).

The instrument that collected the data used for this work is the Mars Orbiter Laser Altimeter (MOLA) (Zuber *et al.*, 1992; Smith *et al.*, 2001). The instrument operated by measuring the light-time-return of a 1.064 µm laser pulse sent from *Mars Global Surveyor*, through Mars' atmosphere, reflected off the surface, and returned to the craft and collected in a 0.5-m parabolic mirror. The instrument had an emission rate of 10 Hz for each 8 ns pulse which, based on the average orbital speed, resulted in an along-track footprint spacing of ~300 m while each footprint was ~160 m in diameter due to spreading; inaccuracies in spacecraft orbit reconstruction result in uncertainties of ~100 m of where the footprint is centered. The across-track spacing varied significantly with latitude but was generally <2 km at the equator and

smaller closer to the poles. Range resolution was approximately 0.37 m though vertical accuracy is ~1 m due to spacecraft orbit uncertainties (Smith *et al.*, 2001). The instrument operated for several years before it failed and was used as a passive detector after having returned approximately 595 million topographic measurements that now form its primary dataset (Neumann *et al.*, 2003a, 2003b).

The reduced and calibrated MOLA data are available in two primary formats – point/shot and gridded. MOLA Precision Experiment Data Record (PEDR) is the former and is the actual latitude, longitude, and range to the surface for each 595 million points returned over the operating lifetime of the instrument. Ideally, these are the data that would be used in any analysis because they have undergone the least amount of manipulation. In contrast, the MOLA Experiment Gridded Data Record (MEGDR) is the binned and interpolated MOLA data across the planet. Due to the fidelity of the data, MEGDR is available in up to 1/128° per pixel (~463 m/pix at the equator). Due to the spacecraft orbit, higher MEGDR are available near the poles at up to 1/512°/pix. MEGDR were used in this work (as described below) because MEGDR were searched similarly to THEMIS maps and this required a uniformly gridded dataset. Using PEDR would have required a rough visual interpolation to discern craters independently of the THEMIS markings, defeating the purpose of using PEDR to begin with.

2.3.1. Manual Topographic Measurements

After crater identification and fitting, the second cataloging step was to use MOLA gridded topographic data (Smith *et al.*, 2001) at 1/128° resolution to derive relevant topographic information for each $D \geq 3$ km crater. The height of the rim, elevation of the surrounding surface, and greatest depth of the crater cavity were recorded. This was done in *Igor Pro* software using custom-built algorithms. Manually, an *N*-dimensional polyline was created that identified points along the crater rim. A second polyline was created to identify the surface outside of the crater and its ejecta to estimate the pre-impact surface elevation; this was the most prone to uncertainty. A third polyline identified the lowest points in the floor of the crater.

Because of the non-idealities of the Martian surface (*e.g.*, craters often overlap other topographic features or each other), this is a step that cannot yet be effectively performed with the same accuracy by an automated algorithm.

From these three polygons, the average rim height, average surface elevation, and average crater floor depth were calculated along with the standard deviations as an estimate of the uncertainty in these measurements. MOLA MEGDR count data were used to eliminate gridded points with 0 actual PEDR points that went into them. In addition to the topographic information, NLLS circle and ellipse fits were performed from the rim polygons to serve as a verification and validation of the THEMIS-based diameters (see Section 2.3.4 for a discussion of this comparison). The total number of points of the polygons (as well as the polygons themselves) were also saved so that: (1) A researcher may exclude from further analysis craters that had less than a certain number of points identifying, for example, the rim; (2) if different or better algorithms for determining circle or ellipse fits are created in the future, they can easily be run on the polygons without needing to recreate them; and (3) it allows for spot-checking of random and outlying craters for both self-consistency and consistency between different researchers. Keeping track of this information and the uncertainties associated with each parameter in the new database allows for a more robust statistical analysis than has previously been done. This has not been included in other crater databases and will be of benefit to the user of the final, released product.

This step could not be performed for all craters due to the coarser resolution of the MOLA gridded data compared with THEMIS. The final cut-off is that craters $D < 3$ km were not analyzed due to the inherent data limitations as discussed below and in section 2.7.2. Any craters that either (a) cannot be seen in the MOLA data, or (b) have too few non-interpolated pixels to be accurately analyzed (generally fewer than 5-10 pixels across) were also not analyzed in this step.

The approach described above is different from what some researchers have done in the past. Notably different is that topographic data were used in lieu of photoclinometric and

shadow techniques (*e.g.*, Davis and Soderblom, 1984; Pike, 1988). But even from topographic data, different researchers use a somewhat different definition of rim height and floor depth, namely using the maximum elevation along the rim and the minimum depth in the floor instead of an average (Stepinski *et al.*, 2009). However, the method used here is not without precedence, as it follows that used by the IMPACT program developed by Mouginis-Mark *et al.* (2004), or other manual methods such as those by Boyce *et al.* (2005).

2.3.2. Using Gridded Versus Spot MOLA Topography Data (MEGDR vs. PEDR)

Potential questions with regards to the original location of the MOLA data points arose when using the MEGDR data. While many unmistakable artifacts from poor coverage in areas were avoided, a separate analysis of the topographic derivation by using the original spot data in a few locations was performed: The entire PEDR data record comprises roughly 595 million points (Neumann *et al.*, 2003a), and even when culled to just latitude, longitude, and elevation, it takes over 14 GB of disk space and brings standard modern workstations to a crawl. Consequently, craters on 1/8 of the planet were compared, corresponding to two of the regions in which the 1/128° MEGDR data are available. The first is a near-equatorial region, 0°-90° E and 0°-44° N. The second is a polar region, 180°-270° E and 44°-88° S.

The saved polygons from the main MEGDR topographic analysis were used. A nearest-neighbor search was performed for the closest PEDR point that matched a polygon vertex from the ~39 million PEDR points in each region. An arbitrary threshold that the closest PEDR point must be within 2 gridded pixels in MEGDR was set (1/64°, or 926 meters at the equator). If the closest was beyond this, then the original polygon point was eliminated from this test. Any duplicates were also eliminated (since two vertices could have the same closest PEDR point). With the new topography points from PEDR for the crater rim, surrounding surface, and crater floor, the same topographic analysis was performed: Mean elevation and standard deviation each were calculated for the rim, surface, and floor points.

To estimate the robustness of using MEGDR versus PEDR, the magnitude of the

difference of the means for the two rims (MEGDR and PEDR), surfaces, and floors values was analyzed. It was compared with the $\mu \pm \sigma$ calculated from the MEGDR analysis to determine if they were within the original estimated uncertainty range. Overall, the differences were on the scale of 10s of meters with 50% of the 17,190 craters having rim elevation differences <8.0 m, surface differences <5.8 m, and floor elevation differences <3.2 m. 95% of the craters had rim elevation differences <40 m, surface differences <41 m, and floor differences <32 m. When comparing the differences with the standard deviation computed for the MEGDR means, 0.94% were larger than the standard deviation for surface elevation, 0.13% had surface elevation differences larger than the standard deviation, and 10% had floor elevation differences greater than the standard deviation. Given the meaning of a "standard deviation" being one would expect ~68.3% of the data to fit within it, results of 10% for the floor, <1% rim, and ~0.1% for the surrounding surface indicates using MEGDR as described above is reliable.

No significant trend with crater diameter was observed. The only one observed was that the largest outliers - where the differences between the MEGDR and PEDR elevation means were greatest - were for the smallest craters (as expected; see section 2.3.3 below); but, these were outliers and no statistically significant trend line could be fit through the mean difference as a function of diameter. Additionally no significant trend was observed in the offset as a function of latitude except at latitudes poleward of ~75° where the differences from the two data sources became less, likely due to the significantly higher point density.

As a test of the initial nearest-neighbor assumption, both regions were again analyzed but had the neighbor threshold changed to 1 MEGDR pixel (1/128°, or 463 m at the equator). The results were nearly the same, though differences were slightly larger (~5-10 m for 50% of the craters and 40-55 m for 95% of the data; the percentages with differences larger than the standard deviations were statistically identical).

From these analyses, it can be concluded that using the 1/128° MEGDR data sets, when avoiding clear interpolation artifacts, yields statistically identical results to using PEDR data for this kind of topographic analysis.

2.3.3. Robustness of MOLA Gridded Data Compared with Point Data

Some may argue that MOLA data are not practical for analyzing crater topography for diameters smaller than ~6-10 km (Boyce (pers. comm.) and Mouginis-Mark (pers. comm.)). In some cases, this is clearly true, especially with automated methods, due to two main reasons. First, simple gaps in the MOLA coverage result in interpolation that smooths the MEGDR and decreases topographic relief (*e.g.*, Mouginis-Mark *et al.*, 2004). However, these are usually easily avoidable because they are fairly clear when encountered. The second is more insidious: The MOLA instrument recorded data with an along-track spacing of ~300 m and had a surface spot size of ~160 m (*Smith et al.*, 2001). For smaller craters, on the order of 5 km, this could result in (a) the instrument missing the deepest portions of the crater floor, and (b) the instrument missing the crest of the crater rim. In either of these cases, a subdued crater profile would be derived and there is no obvious indication from the data that this would be in err. This is a situation where photoclinometric and shadow methods would likely obtain superior results *if* the surface has a uniform albedo.

To roughly characterize this potential offset, three pairs of craters $D \sim 5$ and ~ 20 km were selected at random from regions around 0°, -40°, and -80° North latitude and were examined with PEDR data overlaying THEMIS mosaics. An example at each diameter is shown in Fig. **7**. The MEGDR data that were used to identify the rims in roughly half the cases were found to fall within 2 pixels of the THEMIS rim crest, a distances chosen because that is comparable to the spot size of the MOLA footprint (there were significantly more at higher latitudes). When eliminating the rim points that did not have a PEDR point within that 2 THEMIS pixel tolerance, the rim heights calculated were affected by ±25 m at 0°, ±20 m at -40°, and ±10 m at -80°. These were all within the stated standard deviation recorded from the original MEGDR analysis. These indicate that rim heights in this database are reliable estimators given the MOLA data fidelity. Future work using HRSC (High-Resolution Stereo Camera aboard *Mars Express* (Neukum *et al.*, 2004; Gwinner *et al.*, 2010)) digital terrain models at ~100 m/pix scale may indicate the reliability of measurements on smaller craters.
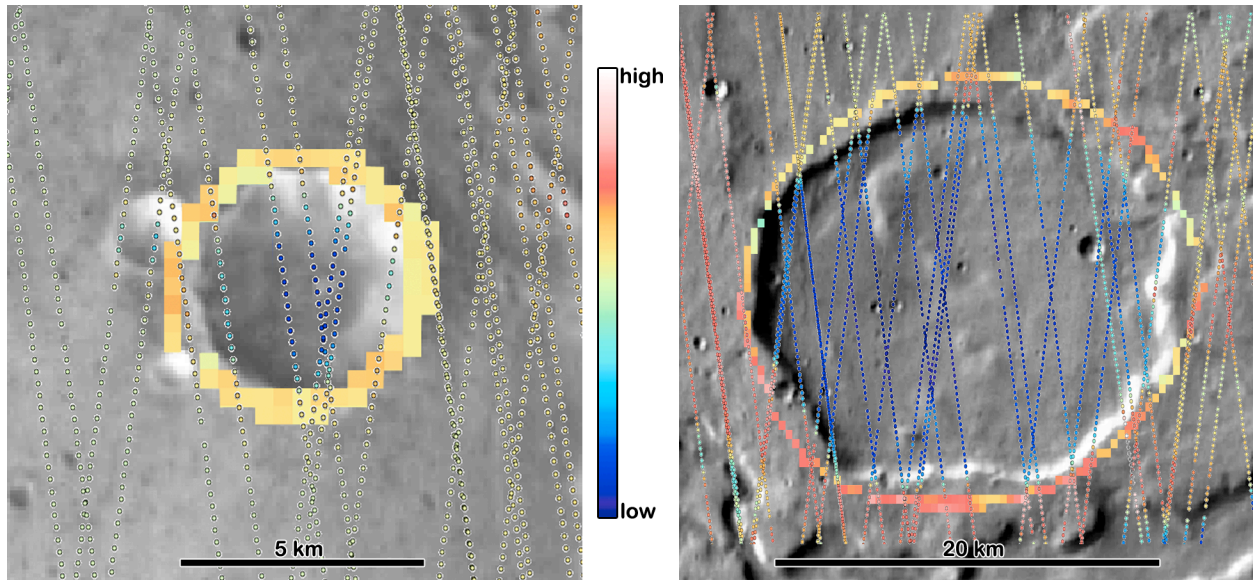
Figure 7: Images showing two craters with MOLA PEDR and MEGDR data overlaid. Left crater is $D = 5.8$ km (-1.5°N, 102.1°E) and right crater is $D = 21.1$ km (-40.1°N, 173.5°E). The background image is THEMIS Daytime IR mosaic. Colored squares around the rim are the MEGDR data that were used to define the rim height in the main topographic analysis. Smaller colored circles show the PEDR tracks. Where a circle does not overlap a square, the MEGDR data point had no actual data and was purely interpolated. All PEDR points are shown, but only those that were within two THEMIS pixels of the crater rim were used in the comparison analysis in this section.

Because of this, and since the MOLA data can resolve craters down to $D \sim 3$ km, this entire range was utilized for this catalog. Though the results may be slightly subdued, and individual persons may opt to not use them if they choose to use this catalog, they are still included and their aggregate results are used in the companion paper, this volume (Robbins and Hynek, 2011c).

2.3.4. Comparing THEMIS- and MOLA-Derived Diameters

Agreement between THEMIS- and MOLA-derived crater diameters is fairly good throughout the database. Fig. **8** top panel illustrates the absolute difference between these two values and Fig. **8** bottom panel shows the relative difference. In these, there is a slight discontinuity in the binned values at the 5-km point. This is because craters were analyzed in MOLA data first for all THEMIS diameters $D \geq 5$ km and then $3 \leq D < 5$ km. Besides this, an internal consistency was used for craters $D \geq 5$ km where a MOLA-derived diameter needed to be within ±25% of the THEMIS value to not be rejected (the assumption being that interpolation
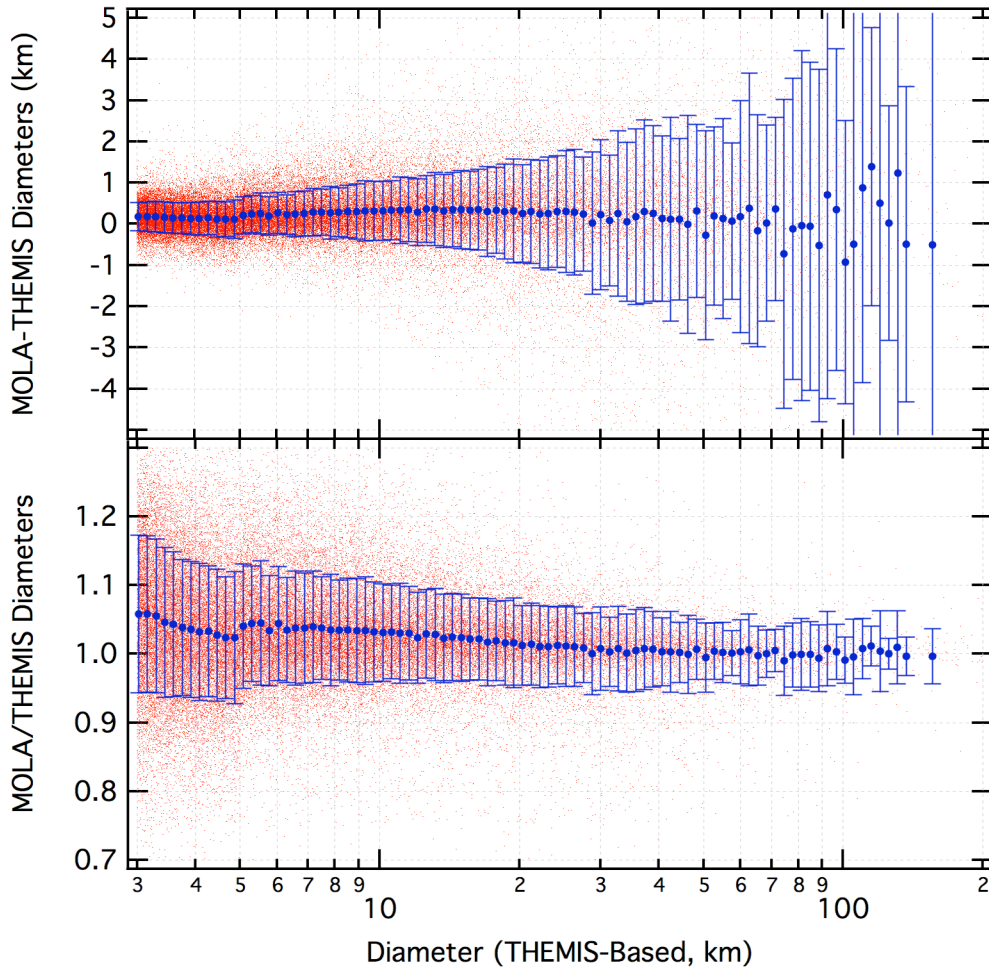
Figure 8: Each point is a single crater comparing the THEMIS- and MOLA-measured diameters. Data have been binned in multiplicative $2^{1/16}D$ intervals with means and standard deviations displayed for the craters in that bin. Graphs are cropped to show regions of interest and statistical significance. See text for explanation of discontinuity at 5 km. Top Panel - Absolute difference between THEMIS- and MOLA-derived crater diameters. The values are slightly above but still very close to 0, indicating that MOLA generally resulted in slightly larger crater diameters by an average of ~0.25 km over most diameter ranges. Bottom Panel - Relative difference between THEMIS- and MOLA-derived crater diameters. Over all diameters, the 100% parity is maintained within the standard deviation, though there is a distinct trend towards larger MOLA results at smaller diameters.

artifacts and/or little to no topographic relief masked the crater in MOLA data). For the $3 \leq D < 5$ km range, this was modified to be ±50% because it corresponded to a less significant absolute difference.

Despite this change at the 5-km point, the data clearly show reasonable agreement between the two methods. In absolute terms, ≥68% of the craters are within 1 km agreement in the two measurements at all crater sizes. Considering the level the uncertainty from the NLLS

circle fit to the THEMIS rims from Section 2.2.4, this a more than acceptable spread. While the offset is reasonably constant without a statistically significant trend away from ±0 (although the means are consistently >0 for $D \lesssim 30$ km), this means that the relative difference shows a distinct trend towards >100% (parity) as diameters get larger (Fig. **8** bottom panel). In fact, it is well represented by the power law $D_{\text{MOLA/THEMIS}} = 1.00 + 0.41 D_{\text{THEMIS}}^{-1.52}$. While this is fairly minor even for $D = 3$ km craters (aliased to larger diameters by 5%), it is statistically an important effect to keep in mind, not just when using these for analysis but also when exploring the effects of resolution limits on relatively small features. For example, the Stepinski *et al.* (2009) MOLA-based crater catalog shows a statistically significant increase in number of craters for ~3.5 < D < 7 km over both this database and the Barlow database (Barlow, 1988). This comparison issue is explored in greater detail in section 2.7.5.

2.4. Crater Interior Morphology and Degradation State Classification

Basic size-dependent crater morphology was recognized as early as 1893, by the head of the United States Geologic Survey, G.K. Gilbert (Gilbert, 1893), and was in use by the community within a century (*e.g.*, Dence, 1968; Cintala, 1977; Wood, 1978; Melosh, 1989). This crater database follows that basic schema and adds to it. The database contains three columns of interior crater morphology: The first column is the basic crater type, the second notes any features of interest in the crater walls, and the third column notes features upon the crater floor. Appendix C provides archetypal examples of morphology types used. Additionally, there are three more columns of information for each crater that can be loosely classified as "morphology." The first is the degradation state (sometimes referred to as preservation(al) state or modification state) which is how fresh or eroded the crater appears. Second is a subjective confidence measurement of how certain the authors are that the feature identified is actually an impact crater. Third is another subjective measurement of how likely the identified crater is a secondary crater. If it is identified as a probable secondary, the catalog ID of the primary is included if it can be determined. These are explained in detail in the following subsections.

2.4.1. Basic Crater Types

All craters were visually inspected to determine morphology in 100 m/pix THEMIS mosaics with rare assistance from ~5-7 m/pix CTX images (ConTeXt Camera from Mars Reconnaissance Orbiter (Malin *et al.*, 2007)). Craters were first categorized based on simple gravity-controlled shape and abbreviated with three letters: Simple (Smp), complex (Cpx), and basin (Bsn). Simple craters are bowl-shaped. Complex craters are characterized by the presence of central peaks/rings, wall terraces, and/or a flat floor (Melosh, 1989). The basin classification was used for any crater larger than ~500 km in diameter; there is no agreed-upon transition diameter for where a large crater becomes a basin except in the case of multi-ring basins, such as Orientale on the Moon (Mars does not have any obvious present-day examples of these). Differentiating between a simple and complex crater was not attempted in all cases. For example, a partially filled simple crater will have a flat floor and become fairly identical morphologically to a small pristine complex crater that originally had a flat floor. For such cases, this column was left empty under the philosophy that it is better to omit than to provide wrong information.

Additional letters were sometimes appended; in the simple-complex transition range ($5 \lesssim D \lesssim 8$ km), the additional letters may be present *without* Smp or Cpx preceding them. These are based on the morphologic types identified in Barlow and Bradley (1990) and are used to indicate: Flat Floors (FF), Central Peaks (CPk), Central Pits (CPt), Summit Pits (SuPt), Peak-Ring (PkRg) (observed nine times), Unclassifiable/Chaotic (Unc), and "Central Mesa" (CMa) (observed nine times). In this manner, a complex crater with a summit pit will be listed as "CpxSuPt." The Unc type was used when it was not possible to identify characteristics of the original floor of the crater due to subsequent infilling or fracturing. FF craters were only indicated for the complex type, as simple morphology always forms as a bowl but later modification may give it a flat floor. Not infrequent were transitional-sized craters that appeared to be simple due to their bowl shape but had central peaks. In these cases, simply a "CPk" was indicated. Finally, the "CpxCMa" designation, indicating a "central mesa," applied to large

craters in the complex size regime that have a mesa-like central region that spans ~50% of the crater's diameter.

2.4.2. Crater Walls

The second interior morphology column notes any features of interest in the crater walls. In the case of multiple features, a backslash ("/") separates multiple items. Possible features identified in the database are: Terraced, Bench (sometimes called "concentric" in the literature), Gullies (at THEMIS resolution), and/or a channel breaching the wall along with the compass direction (*e.g.*, "Channel SE" indicates a channel breaches the southeast wall). If tectonic features such as graben run through the crater and its walls, this is indicated in the floor morphology section, described in Section 2.4.3.

The former two are formational features. Terraces occur in complex craters due to weakness in the target material that leads to fracturing circumferential to the crater rim (Melosh, 1989). Bench/concentric craters are generally small craters that have a rim, a drop to a mid-level "bench" that is fairly flat and extends over a sizeable part of the crater's radius, and then drops to a more typical crater depth for that diameter; this bench extends over the boundary in a layered target of weak (top) and strong (bottom) material before breaching the stronger material towards the center (Melosh, 1989). The latter two are modification features that can occur at any time after the crater has formed. The "gullies" refers to any thin, channel-like pattern that runs down the crater wall at the resolution of the THEMIS maps. This can be simple mass wasting, or it may be due to aquifers bursting (*e.g.*, Malin and Edgett, 2000) or melting from snow deposits (Christensen, 2003). The "Channel" term is *only* used when the channel breaches the crater wall and the channels must be many km long. They may or may not show obvious flow-like features and/or deposits into the crater.

2.4.3. Crater Floors

Additional features of interest on the crater floor were noted in a third interior morphology column (see Appendix C for examples). This includes a generic "Floor Deposits"

that does not presume an origin. Floor Deposits were indicated in any complex crater that did not have a uniform floor texture, was not of the other types, or clearly had a large amount of burial (this would also be reflected in the degradation/modification state). It was indicated in simple craters if the crater rim opened to the surrounding surface and was at the same elevation, or if it was not bowl-shaped.

Other possible values in this column are: Fractured, Channel, Dunes, Valley Deposits, Slump Deposits, Landslide Deposits, Ejecta Deposits (from an external crater), Tectonics, Alluvial Fan (from Moore and Howard, 2005), and Delta (from Di Achille and Hynek, 2010). Fractured indicates a highly fractured crater floor (sometimes referred to in other databases as "chaotic"), and this is separate from Channel that designates a crater that has one or more channels running through it (there must be a visible channel through the crater, not just breaching the wall). Dunes indicates if sand dunes are present. Valley Deposits are where a channel opens into a crater and material appears to have gathered at its mouth. "Slump Deposits" are floor deposits that appear to be the result of mass wasting from the crater rim and/or walls, while "Landslide Deposits" are a sub-class that have a specific fan-like morphology that may be fluvial in nature or triggered by another impact event near the crater rim. "Ejecta Deposits" are cases where another, external crater's ejecta is within the crater of interest; if there is ejecta on the crater floor due to a crater that formed completely inside the crater in question, this was not indicated. "Tectonics" are cases where extensional or compressional features are present in the crater floor, such as graben or wrinkle ridges.

2.4.4. Determination of Crater Degradation States

There is a lengthy history of studying the degradation(al)/modification/preservation(al) states of craters by processes of gravitational mass wasting such as landslides, aeolian deposition and erosion, and fluvial erosion. Selected examples include the use of crater degradation to study gradational epochs (Grant and Schultz, 1990), a broad overview by Grant and Schultz (1993), more detailed studies of crater morphology including topographic dependence by

Craddock *et al.* (1997), and studies of specific regional degradation such as by Barlow (1995).

Classifying the degradation state of craters is where, unfortunately, every researcher has his or her own system. Historically, crater degradation states have been reduced to three or four different classes that range from ghost (craters that are almost completely buried or eroded so they are barely visible) to pristine craters (such as by Craddock and colleagues, *e.g.*, Craddock *et al.*, 1993, 1997). A distinct benefit of this system is that with fewer classes, there is a larger step between each class and consistency is more likely to be maintained. With high-resolution data and data types other than imagery (such as topography and thermal inertia), Barlow (2004) recently advocated for a more detailed eight-class system based on 0-18 possible points a crater can be assigned. These points are based on the crater depth (0-5), rim preservation (0-4), ejecta preservation (0-4), state of the interior (0-5), and relative thermal inertia of the crater's immediate surroundings versus those farther away (0-2). Points are combined and then scaled to give a 0-7 preservation class. This has the benefit of both utilizing disparate data to derive a preservation class and having a system closer to a continuum of degradation states.

Table 1: Schema used to define degradation states ("class") for craters. Craters are classified with three morphologic characteristics and the relative depth from topography (if available). The corresponding rank is converted to a degradation class. The majority of craters in a given class will have characteristics from that row, but that is not always the case. It is possible - if highly unlikely - for a crater to ha, for example, a "Sharp" rim while having no ejecta and being mostly infilled.

Relative Depth	Rim	Ejecta	Interior	Rank[3]	Class
<1/4 (1)	Rimless (1)	None (1)	Mostly Infilled / Highly Modified[1] (1)	4-6 (3-4)	1
¼-1/2 (2)	Slightly Elevated (2)	None (1)	Significant Deposits / Modification[1] (2)	7-9 (5-6)	2
½-3/4 (3)	Some Degradation / Modification[1] (3)	Some Erosion / Modification (2)	Some Infilling / Modification[1] (3)	10-13 (7-9)	3
>3/4 (4)	Sharp[2] (4)	Pristine (3)	Pristine (4)	14-16 (10-11)	4

[1]Modification includes: Gullying/dissection, fracturing, lava flows, ice flows, mass wasting (*e.g.*, from the rim), superimposed cratering, etc.

[2]Does not necessarily mean "pristine" (*i.e.*, can have a small crater superimposed or a very small bit of modification).

[3]Parenthetical values are if depth information is not present.

While the Barlow (2004) system may be more ideal, it is not feasible for the much larger number of craters in this database. Instead, this work uses some of the objectiveness that system suggests, but it has been shrunk in scope to the more traditional four-class system as listed in Table **1**. In using this, some of the simplicity of four-class systems is preserved while also preserving more of the objectiveness with distinct criteria of the Barlow (2004) system.

In this analysis, crater "Relative Depth" was based on the local depth/Diameter ratio rather than a global average. As discussed in the companion paper (Section 3.5) and elsewhere (*e.g.*, Stewart and Valiant (2006)), this is important to take into account because even pristine craters near the Martian poles (poleward of ~±40° latitude) are, overall, significantly shallower than craters closer to the equator. If this were not taken into account, then craters near the poles would consistently be 1 or 2 classes less preserved than their equatorial counterparts which would introduce a significant systematic error.

All intermediate classifications in the rank and class are preserved in-house, but only the final class is included as the DEGRADATION_STATE column in the released crater database.

2.4.5. Is This Crater a Secondary?

Secondary craters are a long-standing problem and debate that has no definite solution nor unified model for its importance. The first step in understanding them is to differentiate between a primary and a secondary crater. In this database, this discrimination is based on classic morphologic characteristics of secondary craters (Shoemaker, 1962; Shoemaker, 1965; Oberbeck and Morrison, 1974; and McEwen and Bierhaus, 2006):

- Is the crater highly elliptical with the long axis oriented towards a much larger crater?
- Is the crater entrained within a chain of craters radial to a much larger crater?
- Is the crater a member of a large group of craters, the overall group shape having a major axis radial to a much larger crater?
- Is the crater surrounded by chevron ejecta that points to a much larger crater?

If a crater in the database fit some of these characteristics, an indication as a possible or

probable secondary crater in the column SECONDARY was made. Values were a trinary N, M, or Y, indicating "No," "Maybe," and "Yes." "Maybe" indicates the crater displays some secondary morphologic characteristics, but it cannot be determined with certainty if it is actually a secondary crater. "Yes" indicates that the crater is a secondary beyond reasonable doubt. Where possible, the CRATER_ID was given following a ";" if the primary for M or Y secondary craters could be identified. For example, if a crater was identified as a secondary and the primary identified as 01-2-34567, then the field SECONDARY would read "Y; 01-2-34567".

2.4.6. Is This a Crater?

In several cases (~1% of the total analyzed), features included in the database are somewhat ambiguous as to whether it is a crater, or if a crater, an exogenic crater (as opposed to, *e.g.*, an endogenic collapse pit crater). The database field CONFIDENCE_IMPACT_CRATER contains, on a scale of 1-4, the subjective probability that the feature identified is a crater. Out of the 78,895 craters $D \geq 3$ km that were morphologically classified in this release, 183 (0.23%) were listed as 1, 378 (0.48%) as 2, 683 (0.87%) as 3, and the remaining 98.42% as 4. This amount of uncertainty is well within the variance between researchers (Lissauer *et al.*, 1988).

2.5. Crater Ejecta Morphology Classification

Fresh craters and those with light to moderate degradation/modification will display ejecta surrounding the crater rim. Typically, continuous ejecta blankets will extend to ~1 crater radius from the crater rim while additional rays of ejecta can travel much farther (*e.g.*, Tycho Crater's ejecta on the Moon has been mapped half-way across the body (Wilhelms and El-Baz, 1977)). On the Moon and Mercury, simple radial ejecta where the material was ballistically emplaced from the excavation of the crater cavity is the only type observed. Throughout the literature, this has been referred to simply as "radial," and this database follows the recommendations of Barlow *et al.* (2000), abbreviating it as "SLERd" (single-layer ejecta, radial). Examples of ejecta types discussed here are found in Appendix D, and a preliminary discussion of these ejecta types is addressed in the companion paper (Robbins and Hynek, 2011c,

this volume (Section 3.3.3)).

From the first spacecraft images returned of Mars, a new ejecta type was observed that was comprised of one or more cohesive layers of material. Throughout the literature, these have been referred to under a diverse range of names, including flower (Costard, 1989), composite (Johansen, 1979), and various Types and Classes (*e.g.*, Mouginis-Mark, 1979; Blasius and Cutts, 1980; Horner and Greeley, 1987; Costard, 1989). The Mars Crater Morphology Consortium convened in the late 1990s to codify a set of recommendations for a standardized nomenclature for these features (Barlow *et al.*, 2000), and with only very slight modifications, that is used in this database.

This database contains five fields for every crater that describe ejecta if it is present for the crater and if that column relevant. The first is NUMBER_LAYERS and if present has a value ≥ 1 describing the number of layers of *cohesive* ejecta (simple radial ejecta is not included in this count). The second is MORPHOLOGY_EJECTA_1. For radial ejecta, "SLERd" is in this column. For the cohesive layered ejecta, the Barlow *et al.* (2000) nomenclature is followed: Layered ejecta (LE) displays several morphologic sub-types that are used in its five-letter classification. The first is how many layers of ejecta are present – a single layer (SLE), two (double) layers (DLE), or three or more layers (MLE). The second main type discriminator is if the ejecta terminates in a rampart it has an R as the fourth letter; if not, it is termed "pancake" and the P is the fourth letter. If *any* part of the ejecta edge displays a rampart morphology, even if the rest does not, the R designation is given in lieu of P in this catalog. Third is how the edge of the ejecta terminates, whether it is sinuous or fairly circular. The lobateness factor Γ defines this as:

$$\Gamma = \frac{\text{area of ejecta}}{\pi \left(\text{radius of circle with equivalent area}\right)^2} \tag{3}$$

If $\Gamma \leq 1.5$, the ejecta is circular (*e.g.*, SLEPC). If $\Gamma > 1.5$, the ejecta is sinuous (*e.g.*, SLERS).

Barlow *et al.* (2000) also recommended that when multiple types of ejecta are present around a single crater, the terms be combined. For example, a crater that displays one continuous layer of ejecta in addition to radial ejecta would be designated "SLERSRd." It is on

this point that this database deviates from those recommendations. Instead, a backslash ("/") is used to indicate multiple classifications for multiple layers. This is done for expandability and to provide better information. For example, a class of craters found in the mid-northern latitudes is DLE, but the inner layer is PC while the outer is RS. Hence, this is designated as "DLEPC/DLERS" in this database. In another example, sometimes there will be a radial ejecta component between two cohesive ejecta layers. Pure radial non-cohesive ejecta is *not* considered a layer in the S/D/M classification, so in this case the designation would be "DLEPC/DLERd/DLERS."

The third ejecta morphology field describes the overall texture of the LE blanket and it provides additional information about its edge; this is found in `MORPHOLOGY_EJECTA_2` as a two- or four-letter code. The first two letters are either "Hu" or "Sm" which stand for "hummocky" and "smooth" to describe how the ejecta blanket appears in THEMIS Daytime IR data. These two are always present in this column if there is a layer of ejecta present while there may or may not be an additional two letters used. If present, they are "BL," "SL," "Am," or "Sp." These stand for "broad lobes," "small lobes," "amorphous," and "splash." "Broad lobe" is used when the separation between different lobes of a layer is more than 50% of the extent of the layer; this is measured by eye and is not an exact delineation. "Small lobe" is where the terminus of the ejecta is more of a serrated "crinkle scissor" type, though it is more precisely defined as when the separation between these serrations does not extend more than 50% of the extent of the ejecta (this is also not exact). The "amorphous" type is for an overall ejecta shape that is generally asymmetric, blobby, "amoeboid"-like. "Splash" is when the ejecta appears as a splash onto the surface with the ejecta generally extending far from the crater rim but separated into many different strands.

A final, optional, fourth column `MORPHOLOGY_EJECTA_3` was occasionally used to describe unique shapes of ejecta blankets. These types are: Butterfly, Rectangular, Splash, Bumblebee, and Pin-Cushion. In addition to these, "Pseudo-Butterfly" and "Pseudo-Rectangular" are occasionally used to describe the ejecta around a single crater. Occasionally, a

binary impact will occur and the two craters overlap, their touching rims being straight between the two. In this case, there may be cohesive ejecta that appears to be squeezed between the two in which case "bumblebee" is used for both craters. Finally, even if there is no ejecta but the crater is at the head of what on Earth would be considered a sandbar, the term "Sandbar" is placed in this column of morphology. Examples of these are all found in Appendix D.

Butterfly ejecta occurs around a fairly elliptical crater. This ejecta will have a zone of avoidance at the edge of the crater at one end of the major axis; this avoidance zone typically covers ~120-130° (Robbins and Hynek, 2011c). The ejecta has the farthest extent from the crater almost immediately past this zone, and it stays relatively far from the rim throughout most of the length of the crater. It will narrow as it approaches the other end of the major axis and have nearly a similar zone of avoidance, though it will still be present in a substantially reduced extent. It will typically have one or two "tendrils" extending beyond this. If the ejecta is similar but does not, for example, have a total zone of avoidance, does not nearly disappear at the other end of the major axis, or if the ejecta does not have an obvious farthest extent immediately past the zone of avoidance, the ejecta is considered "Pseudo-Butterfly." Seventy-one craters were classified as having butterfly ejecta, while 98 were classified as pseudo-butterfly.

Rectangular ejecta may have a similar genesis to the Butterfly type, but it has a nearly 180° zone of avoidance at both ends of the major axis, and it will extend a nearly constant distance from the crater's edge along the rest of the crater. The Splash type is the same as the "Sp" suffix in the second morphology classification. Pin-Cushion ejecta is exclusive to the ─-PC (first morphology column) and Hu (second morphology column) type. In the THEMIS Daytime IR mosaics, this crater appears to be bulbous with a pitted texture, appearing at the THEMIS 100 m/pix data to resemble a pin cushion. This may be due to overlying radial ejecta as this often had a `MORPHOLOGY_EJECTA_1` classification of "SLERd/SLEPC," although this only became apparent at the higher 100 m/pix data and was not clear in the 230 m/pix mosaics.

In all of these morphology information columns, a single value applies to all layers of ejecta for that crater. If there are multiple layers that have a distinct morphology, then

backslashes ("/") are used to separate them with the innermost layer first, second listed second, and so on for the first two morphology columns; it is specified in the third morphology column to which layer the designation applies. If there are, for example, three layers of ejecta where the inner and middle are sinuous rampart, the outer is circular pancake, all are hummocky, the inner has "short lobes" while the middle and outer has broad lobes, and the inner is of the butterfly type, the columns would have the following information:

1. MLERS/MLERS/MLEPC

2. HuSL/HuBL/HuBL

3. Inner is Butterfly

Finally, there is a comments column `MORPHOLOGY_EJECTA_COMMENTS` that may contain additional information about the ejecta. An example that was frequently used is, "There may be a cohesive layer within the Rd ejecta."

2.6. Crater Ejecta Morphometry Measurement

While the morphologic crater ejecta classification is somewhat subjective, this database also contains an objective measurement of ejecta blankets of the cohesive layered ejecta type in all cases where this could be measured. Due to some image clarity, completeness, and indistinct contacts, it was not possible to measure all ejecta.

2.6.1. Outlining Ejecta and Calculating Their Properties

Ejecta were identified in THEMIS Daytime IR global mosaics and outlined with 1 vertex every 500 m, identically to how crater rims were traced as described above. A note was made in the *ArcGIS* shapefile designating the ID of the crater that the ejecta shape belonged to. These were then imported into *Igor Pro* software along with the already processed crater rim data. Using the same algorithms as with the crater rims, the ejecta outlines were projected from decimal degrees to kilometers from the centroid after factoring in the spherical surface of Mars. After this, for every outline, the following data were calculated and stored to the designated database columns (where # refers to a number between 1 and 5, inclusive):

- `LAYER_#_PERIMETER`: Perimeter of each outline (units are km).

- `LAYER_#_AREA`: Area of each outline using a standard geometric method for the area of an irregular polygon:

$$A = \frac{1}{2} \sum_{i=0}^{n-1} \left(x_i y_{i+1} - x_{i+1} y_i \right) \tag{4}$$

  where n is number of vertices, x is longitude, and y is latitude. The ideal area of the crater (πr^2) is subtracted, and the final area of the ejecta is recorded (units are km^2).

- `LAYER_#_LOBATNESS`: The lobateness, Γ, is calculated (Eq. 3) (unitless) using the ejecta area before the crater's area is subtracted.

- `LAYER_#_EJECTARAD_EQUIV`: The equivalent ejecta radius (units are km) - also known as "runout distance" - is calculated as:

$$\text{runout distance} = \sqrt{A_{\text{ejecta+crater}}/\pi} - r_{\text{crater}} \tag{5}$$

- `LAYER_#_EJECTARAD_REL`: Relative equivalent ejecta radius is the runout distance divided by the crater's radius and is also known as "ejecta mobility" (unitless).

Ejecta perimeter and area are self-explanatory and are standard definitions. Ejecta lobateness in this sense is similarly a standard definition and has been used for several decades with no modification (*e.g.*, Kargel, 1986). However, it should not be confused with the *number* of flow lobes that are observed, which confusingly is also termed "lobateness" by a few researchers (*e.g.*, Barnouin-Jha and Schultz, 1998). Runout distance and its derived ejecta mobility, however, have had two different definitions. The first is the one used here that uses an average ejecta extent because it offers a characterization of the overall energy and viscosities involved (*e.g.*, Barlow, 2005, 2006). The second is the maximum extent of the ejecta to determine the absolute farthest the cohesive ejecta could flow given the impact energy available (*e.g.*, Mouginis-Mark, 1979; Costard, 1989). Unfortunately, the two are not easily relatable, and the data would need to be re-processed using the other definition for a meaningful comparison.

2.6.2. The "Infinite Coastline of Britain" Problem: Fractal Nature and Differing Resolutions

A limitation of the utility of ejecta perimeters, areas, and lobateness is the inherent fractal nature of the shape studied and limits of resolution - both the imagery used and the frequency of vertices in the polygons created to represent them. This was first formalized in 1967 by fractal pioneer Benoît Mandelbrot who described it in terms of measuring the coastline of Britain (Mandelbrot, 1967). He found a power law relationship between the length of coastline and the length of the side of a polygon to represent the coastline, but the power law exponent varied for different coasts. Similarly, the non-linear problem of perimeter will vary with the complexity of the ejecta, and while a SLEPC ejecta may be well-represented by a single vertex every kilometer, a complex SLERS may require 10 vertices in the same space to properly represent the perimeter at THEMIS resolution. Similarly, 1 vertex every kilometer may work well for a SLEPC blanket surrounding a 20-km-wide crater, but significant resolution artifacts would arise for a similar blanket surrounding a 1-km-wide crater.

Several case studies were performed to illustrate this dependence and its significance. Different SLE ejecta were chosen to represent different sizes and different types. For smaller craters ($D \lesssim 10$ km), CTX data were used to afford higher resolution in this analysis. For these craters, the ejecta was defined by a polygon with vertices spaced every 50 meters (5 and 10 times higher resolution than used for the catalog). In processing, this resolution was reduced in 50-m intervals down to a resolution of one vertex every 5 km. For larger craters, THEMIS Daytime IR images were used. Ejecta was outlined with a vertex every 100 meters and this resolution was reduced in 100-m intervals in the analysis. Table **2** lists the craters used in this study and their properties. Fig. **9** illustrates the lobateness resulting from the different resolutions. Lobateness is graphed because it roughly normalizes the different crater diameters and ejecta types and it is linearly related to the ejecta perimeter.

As is apparent, there is not a predictable power law that can describe the change in lobateness with differing resolution, crater size, ejecta type, etc. The only two conclusions that can be made were apparent *a priori*, namely that craters with larger lobateness continue to have a
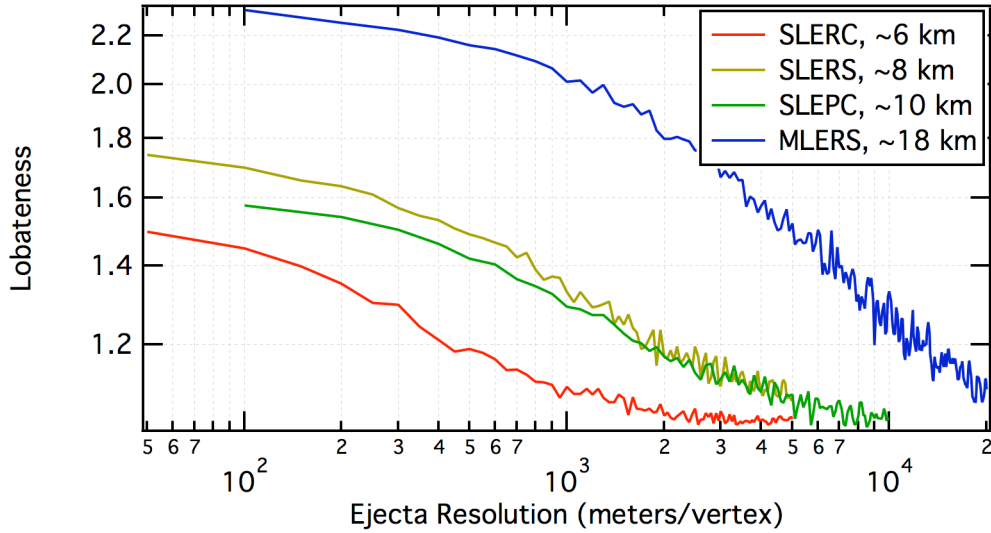
Figure 9: Effect of different resolutions for different crater ejecta morphologies on the derived lobateness. Each type behaves differently as measured by the slope and shape of the curve. Resolution was reduced until there were 10-20 vertices that defined the ejecta perimeter.

Table 2: Craters and properties of the craters used in studying the fractal nature of ejecta.

Crater ID	Diameter	Latitude	Longitude	Ejecta Type 1	Ejecta Type 2
14-1-12282	5.7 km	4.3°	138.2°	SLEPC	HuSL
02-1-06899	8.2 km	5.0°	-152.7°	SLERS	HuBL
14-1-02638	10.3 km	30.3°	108.0°	SLEPC	Hu
14-1-11724	18.0 km	5.4°	102.4°	MLERS[1]	HuBL

[1]Outer ejecta layer was analyzed.

larger lobateness at changing resolutions, and that lobateness decreases with decreasing resolution. Any direct comparison between different databases that have the ejecta outlined in different ways at different resolutions would be arbitrary and inconclusive. The only meaningful comparison is relative (*i.e.*, if the ejecta of crater 1 is larger than that of crater 2 in both databases A and B). Otherwise, the only comparisons that should be made are internal to the database, and even then the ejecta morphometry should only be compared to similarly sized craters (*e.g.*, the values for a 3-km crater will not be reflective of actual morphometry differences relative to a 100-km crater).

2.7. Database Completeness

Completeness of this database is at several different diameters depending upon what information is being queried:

2.7.1. Identified Craters - Statistical Diameter Completeness

The statistical completeness of the database is based upon crater size-frequency distributions: The global database was divided into regions based upon 22.5°x45° latitude/ longitude intervals and an incremental size-frequency distribution was generated from the craters within each bin (based on Arvidson *et al.* (1979), except with multiplicative $2^{1/16}D$ intervals instead of $2^{1/2}D$ intervals; the finer resolution was a reflection of the large number of craters in the database). Completeness was defined to be the next-larger diameter bin after the diameter bin with the most craters within each latitude/longitude region (Fig. **4**). A key assumption of this is that the crater population is well behaved and will continue to increase in number as sizes decrease, at least to diameters significantly smaller than those measured here. Therefore, any decrease observed is due to missing craters in the database rather than a property of the surface.

As a whole, this is a reasonable assumption as previous work has extensively shown that the crater production function increases at least to decameter scales on Mars (*e.g.*, Hartmann, 2005). Locally, this does not always hold. There are a few regions in Fig. **4** that show completeness to diameters >1.0 km. Several of these regions (25% of the planet) were searched again for missed craters, and though craters on the order of ~1% were identified that had not been previously, this could not account for the lower completeness level. It is therefore likely that a geophysical process has acted to remove the ~1-km crater population in these regions at times recent enough such that they have not had time to re-accumulate. In many cases, this was the formation of another large crater and emplacement of its ejecta blanket; in others, aeolian or burial processes likely played a dominant role.

This was especially the case observed around 0°N, 0°E, where several large crater rims were seen with almost no small craters at THEMIS resolution. In the high northern latitudes where Lomonosov and Lyot craters are (65°N, -9°E and 51°N, 29°E, respectively), these craters

and their associated ejecta dominate the region and likely explain the relative paucity of ~1 km craters. The reason these large craters can affect such a broad latitude/longitude bin is (a) they are close to the poles so the bins cover less spatial area, and (b) the crater and its associated ejecta will reset a large area except for craters large enough to remain visible. While craters will have formed since the impact, there may not have been enough time to accumulate enough $D \sim 1$ km craters to affect the size-frequency distribution based on this completeness criterion.

The end result of this analysis is a global mean completeness level of $D = 0.96$ km, with a range $0.76 < D < 1.87$ km when binned at 22.5° latitude by 45° longitude. With the two outlier regions containing Lyot and Lomonosov craters removed, the mean is $D = 0.94$ km and maximum $D = 1.32$ km around the Arabia Terra region. The database as released contains 378,540 craters $D \geq 1.0$ km. The entire database has an additional 252,793 craters $D < 1.0$ km that were removed from this release but may be obtained by contacting the corresponding author.

2.7.2. Topographic Data Completeness

MOLA data resolution is significantly coarser than THEMIS Daytime IR (except near the poles), the limitations of which were addressed earlier in this paper. Because of occasional gaps that were much more deleterious to smaller craters, 100% coverage was not possible. Fig. **10** shows the fraction of craters that could be analyzed with MOLA data as a function of diameter, and this drops precipitously for D≲4 km. (The discontinuity at 5 km is due to different criteria for rejecting MOLA-based measurements for D ≥ 5 km craters and $3 \leq D < 5$ km craters.)

2.7.3. Ejecta Morphology and Morphometry Completeness

In the current release of this database, ejecta morphology and morphometry are complete to 5.0-km-diameter craters ($N = 47,345$). The additional 331,195 craters that are $1 \leq D < 5$ km will be classified and analyzed in a future release.

2.7.4. Crater Morphology Completeness

In the current release of this database, interior morphologies are complete to $D \geq 3.0$ km craters ($N = 78,895$). The additional 299,645 craters $1.0 \leq D < 3.0$ km will be classified and ana-
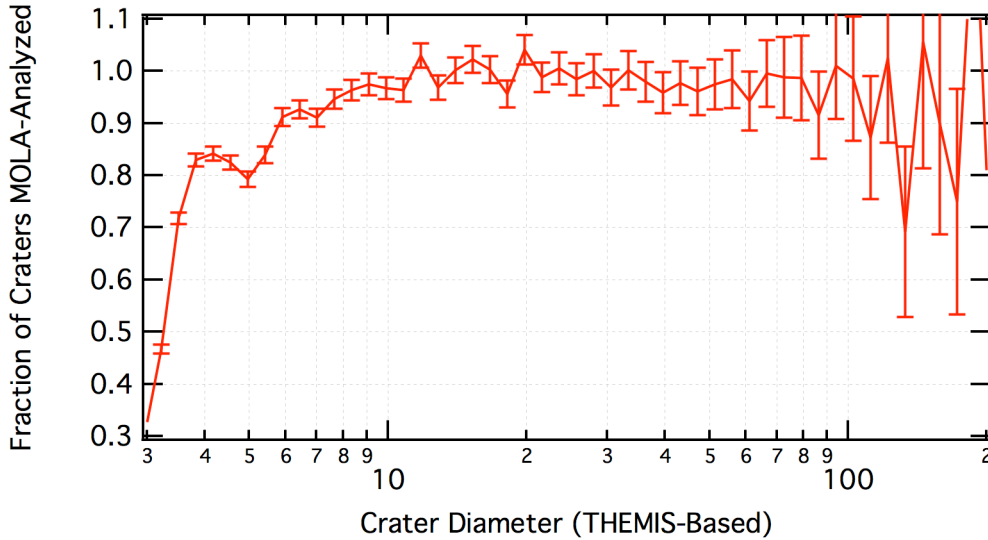
Figure 10: Ratio of a size-frequency diagram of THEMIS-based crater identifications to MOLA-based in multiplicative $2^{1/8}D$ bins. Values above 1.0 indicate more craters were identified in topography than in images; this is solely an artifact of slightly different diameters arising from the two different analyses. Values can get much higher at larger diameters because there are fewer craters per bin, which is why this graph is truncated at 200 km. The fall-off to <50% identification validates the cut-off at 3 km.

lyzed in a future release. However, there are some cases where the morphology is ambiguous, especially in determining the difference between a complex, flat-floored crater or a simple, slightly in-filled or relaxed crater in the ~5-8 km-diameter range. In these cases, the first morphology column was left blank rather than give potentially erroneous information.

Degradation state is similar to ejecta morphology/morphometry and is only complete for $D \geq 5$ km in this release. Secondary crater classification in the current release is only complete for a select grouping of craters analyzed in Robbins and Hynek (2011a, 2011d).

2.7.5. Comparison with Barlow (1989, 2003), Stepinski et al. (2009), and Salamunićcar et al. (2011) Databases

At present, there are three other completed indiscriminant global catalogs of Martian impact craters: The original from Barlow (1988) and her in-progress revision (Barlow, 2003), the automated MOLA-derived Stepinski *et al.* (2009) catalog, and a composite catalog created by correlating several other crater catalogs (Salamunićcar *et al.*, 2011) that undergoes periodic revisions and is currently in version MA130301GT. Barlow's is complete to $D = 5$ km, the Stepinski *et al.*'s claims completeness to $D \approx 3$ km, while Salamunićcar *et al.*'s is $D \approx 2$ km.
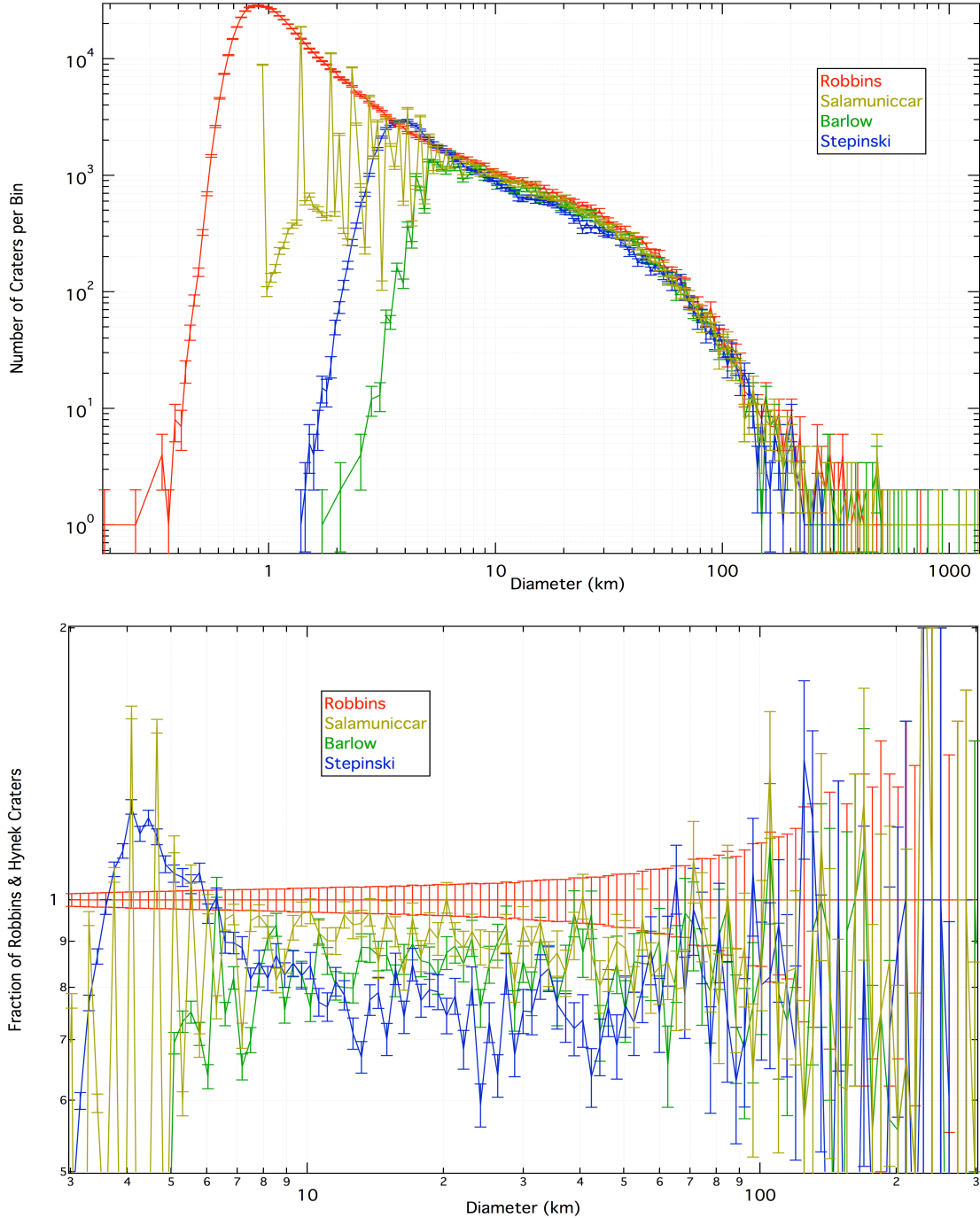
Figure 11: Comparison between four global Martian crater databases with craters binned in $2^{1/16}D$ intervals. The original Barlow database is not complete to $D = 5$ km, though the current in progress version (Fig. **12**) is closer to this work. The Stepinski database displays a marked increase in craters $3 < D < 7$ km, the likely reason discussed in the text. Salamunićcar database relative to this shows good agreement until diameters $D < \sim6$ are reached, at which point their diameters are posterized as discussed in the text. Top - Incremental size-frequency distributions over all ranges included in each database. Note the released database will only contain $D \geq 1$ km craters. Bottom - Ratio of incremental size-frequency distributions relative to the database in this paper. Error bars were calculated by the square-root of the counts in the incremental size-frequency bin divided by the counts in the bin for this database. Note the diameter range is a sub-set of the top panel.
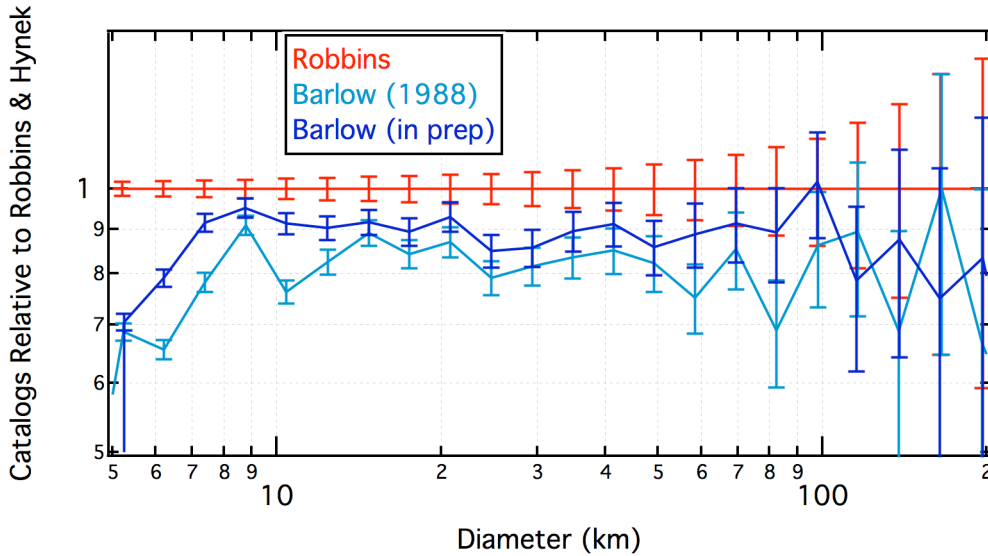
Figure 12: Similar comparison to Fig. **11**, bottom panel, but binned in $2^{1/4}D$ intervals to better show where differences exist and increase number statistics. Horizontal error bars indicate bin width. The "Barlow (in prep)" is a pre-release northern hemisphere catalog supplied by Barlow (pers. comm.) and is unpublished and subject to change.

A detailed comparison of all craters between these three and this catalog is beyond the scope of this paper, but a first-order comparison via an overall crater size-frequency distribution from the four can be done. As shown in Fig. **11**, there is generally good agreement, though over a broad range of diameters ($5 \lesssim D \lesssim 200$ km) this database has slightly more craters. This is likely due to four total searches for craters utilizing multiple datasets as well as the use of the very latest high-resolution THEMIS mosaics. When looking at each catalog, there are marked differences at small diameters.

2.7.5.1. *Barlow (1988)*

The original Barlow database was created before modern computers and displays allowed for image use and manipulation generally taken for granted today. *Viking* 1:2M photomosaic hardcopy maps examined and craters were measured by hand and recorded to create the catalog. *Viking* images on average had the same nominal resolution as THEMIS, but significant spatial variance resulted in a non-uniform image set. Nevertheless, as the first of its kind, the database that has formed the foundation of significant work since its publication contained 42,284 craters including some $D < 5$ km, though it was not claimed to be complete to those sizes. In light of

recent data, a revised version is underway (*e.g.*, Barlow, 2003). When looking at the original catalog, Fig. **11** shows that the original was also not complete to $D = 5$ km. A pre-release of the northern hemisphere was supplied by Barlow and compared in Figure **12** with this database and the original Barlow (1988) catalog. It is more complete than the original, but differences remain where, in general, this catalog has more craters than Barlow's. However, this difference is well within the $1.2 - 1.3\times$ difference between researchers identified by Hartmann *et al.* (1981) and Lissauer *et al.* (1988). Overall, there are 15,812 northern hemisphere craters $D \geq 5$ km in this catalog, 12,920 in Barlow (1988), and 14,200 in the new in prep. edition.

2.7.5.2. *Stepinski et al. (2009)*

The total number of craters in this catalog is 75,919. It was created through an automated computer algorithm that first identifies round, symmetric topographic depressions in the MOLA MEGDR 1/128° product. The next step is to select these depressions and determine whether they are craters through a trained machine-learning technique. There are significantly fewer $D > 100$ basins identified by Stepinski *et al.* (2009) than in the catalog presented here, likely due to significant erosion and superposed features muting the topographic signal of the original crater. However, this cannot explain the discrepancy around $3 < D < 7$ km where the Stepinski catalog makes a sharp increase in crater size-frequency, surpassing even this one at ~6 km, before cresting at ~4 km and decreasing below the number identified here at ~3.5 km. This phenomenon is likely due to the aliasing and nature of the MOLA instrument and data, as described in Section 2.3. For this reason, it is recommended that although the catalog from Stepinski *et al.* (2009) is "statistically complete" to ~3 km diameters, researchers exercise caution at $D \lesssim 7$ km.

2.7.5.3. *Salamunićcar et al. (2011)*

The Salamunićcar *et al.* (2011) catalog and previous iterations were constructed via a semi-automated technique. Previously compiled crater catalogs (such as those in the previous two sub-sections) were used as input. From these, the craters are correlated to determine duplicates, and duplicates are averaged. All output crater candidates are manually verified and

re-measured if deemed incorrect. The final catalog contains all morphometric measurements from the original input catalogs and so this is a true meta-catalog of impact craters. The authors state that global completeness is "up to ~$D \geq 2$ km," containing 85,783 craters $D \geq 2$ km (130,301 craters in total when including smaller diameters). However, the catalog in this paper contains 128,907 craters $D \geq 2$ km alone, 50% more. Thus, while their regional completeness may be to that level, it is far from globally complete to 2 km. In addition, it is difficult to perform a direct comparison between their catalog and this one at smaller diameters because their crater diameters are frequently rounded to odd values: For example, there are 2331 craters listed with diameters 4.16 km, 1300 as 2.924 km, and 10,489 with diameters 1.849 km. This results in posterization on the incremental size-frequency diagram displayed as Fig. **11**; a cumulative diagram retains this effect and so is also inadequate for a comparison.

2.8. Conclusions and Database Availability

We have completed the first global Mars crater database that is statistically complete to 1-km-diameter craters, numbering 378,540 entries, and it will be available for public release shortly. The database was manually generated by detailed examination of THEMIS Daytime IR mosaics at 232 m/pix and 100 m/pix scales as well as from MOLA gridded data at 1/128° per pixel (463 m/pix). It is the first to make use of global 100 m/pix THEMIS mosaics that allowed us to provide unprecedented coverage. The MOLA data used for topographic analysis is the *de facto* standard (*e.g.*, Mouginis-Mark *et al.*, 2004; Stepinski *et al.*, 2009) and we include several topographic measurements along with derived products in the catalog (*e.g.*, the rim height above the surface).

The database contains a robust set of statistical uncertainties in basic crater properties, and overall statistics and confidence intervals are described in this paper. Besides basic positional, size, and topographic depth information, this database contains detailed morphologic and morphometric ejecta properties, interior morphologic indicators, and modification state information for each crater (to a certain diameter limit in this release, as discussed in the text)

(see Appendix A for all data columns included).

The catalog compares well over a large range of crater diameters with other published catalogs. Analysis of this vast catalog is underway, as illustrated in our companion paper (Robbins and Hynek, 2011c, this volume) where we illustrate global crater distributions as a baseline before examining morphologic distributions and then re-analyze the simple-to-complex transition and depth-to-diameter scaling laws. Pending review, we will be making this database freely available for download via the Mars Crater Consortium section of USGS's PIGWAD server (http://webgis.wr.usgs.gov/pigwad/down/mars_crater_consortium.htm). We are also making a web-query site that allows users to download craters and features based on user-selectable fields and options that will be available at http://mars.sjrdesign.net.